Nanoscale Research Letters

NANO EXPRESS

Open Access

Graphene Oxide-Doped MgO Nanostructures for Highly Efficient Dye Degradation and Bactericidal Action

M. Ikram[1*], T. Inayat[2], A. Haider[3], A. Ul-Hamid[4*], J. Haider[5], W. Nabgan[6], A. Saeed[7], A. Shahbaz[8], S. Hayat[9], K. Ul-Ain[9] and A. R. Butt[2]

Abstract

Various concentrations (0.01, 0.03 and 0.05 wt ratios) of graphene oxide (GO) nanosheets were doped into magnesium oxide (MgO) nanostructures using chemical precipitation technique. The objective was to study the effect of GO dopant concentrations on the catalytic and antibacterial behavior of fixed amount of MgO. XRD technique revealed cubic phase of MgO, while its crystalline nature was confirmed through SAED profiles. Functional groups presence and Mg-O (443 cm^{-1}) in fingerprint region was evident with FTIR spectroscopy. Optical properties were recorded via UV–visible spectroscopy with redshift pointing to a decrease in band gap energy from 5.0 to 4.8 eV upon doping. Electron–hole recombination behavior was examined through photoluminescence (PL) spectroscopy. Raman spectra exhibited D band (1338 cm^{-1}) and G band (1598 cm^{-1}) evident to GO doping. Formation of nanostructure with cubic and hexagon morphology was confirmed with TEM, whereas interlayer average d-spacing of 0.23 nm was assessed using HR-TEM. Dopants existence and evaluation of elemental constitution Mg, O were corroborated using EDS technique. Catalytic activity against methyl blue ciprofloxacin (MBCF) was significantly reduced (45%) for higher GO dopant concentration (0.05), whereas bactericidal activity of MgO against *E. coli* was improved significantly (4.85 mm inhibition zone) upon doping with higher concentration (0.05) of GO, owing to the formation of nanorods.

Keywords: Graphene oxide, MgO, Nanorods, Dye degradation, Antimicrobial activity

Introduction

Water is the most essential component for the survival of living creatures. Large scale industrialization and increasing global warming with the passage of time is declining clean water level rapidly. Earth's surface is covered with 71% of water where rivers, lakes and fresh ground water accounts for only 0.03% of the total water, which is deemed useful for drinking [1, 2]. 2.5% of water is worthy of consumption, while the rest of the 97.5% is salty water; therefore fresh water supply is in shortage relative to high demands. Approximately, 750 million population of earth is facing clean water shortage and an increased number of micro-pollutants in water have become hazardous for the ecosystem. The world is facing catastrophic consequences caused by environmental and water pollution. Industries are the main source of water pollution owing to discharged wastewater injected with harmful and potentially toxic compounds. Different industries such as textile, paper printing, and food industry use aromatic compounds that can easily dissolve in water causing water pollution and health hazards [3]. Rapid industrialization and urbanization have caused significant environmental pollution through heavy metals that are persistent in the environment. Adverse exposure to heavy metals in the environment is a serious hazard to living creatures [4]. According to WHO, maximum

*Correspondence: dr.muhammadikram@gcu.edu.pk; anwar@kfupm.edu.sa
[1] Solar Cell Application Research Lab, Department of Physics, Government College University Lahore, Lahore 54000, Punjab, Pakistan
[4] Core Research Facilities, King Fahd University of Petroleum & Minerals, Dhahran 31261, Saudi Arabia
Full list of author information is available at the end of the article

permissible limit of metals in water are, for example, iron (0.1 mg/L), calcium (75 mg/L), magnesium (50 mg/L), copper (1 mg/L) and lead (0.05 mg/L). USEPA reported toxicity profile of heavy metals include lead (damage/fatal to brain), cadmium (kidney damage) and chromium (respiratory tract problems) [5]. The toxic dyes are endangering aquatic lives by blocking sunlight which is necessary for the growth of living organisms. Aquatic species consume these poisonous dyes while these species in turn are consumed by people damaging their health [6].

Various traditional approaches for extracting dyes from wastewater have been suggested, including, evaporation [7], solvent extraction [8], coagulation [9], ion exchange [10], membrane separation [11], physical, chemical and biological techniques [12]. The major problem is that these conventional treatment techniques are expensive when it reaches large scale level. In view of this, researchers have developed various adsorbents such as zeolite, activated carbon, carbon nanotubes, polymers and graphene materials. Adsorption method is extensively used in wastewater treatment to degrade reactive dyes [13–17]. A proper dyes treatment, such as adsorption and catalytic degradation are proposed for dyes removal to improve life quality. Adsorption is cost-effective but catalyst recovery is still a problem that can produce hazardous materials. Catalytic degradation is slightly costly; however it is relatively simple and has the advantage of recyclability [18]. Numerous oxide semiconductors (TiO_2, ZnO, MgO, Fe_2O_3 and WO_3) have been extensively reported as catalysts for organic dye degradation because of their high chemical stability, toxic-free nature, high activity, and cost benefit.

Among these, non-toxic and cost-effective MgO has been shown to be effective in the areas of adsorption, catalysis for polluted water, superconducting products and antibacterial materials [19–21]. Over the last few years, various nanostructures of MgO, containing nanoparticles, nanoflowers and nanosheets have been fabricated successfully [22]. Recently, MgO with a large band gap of 7.8 eV have revealed a lot of interest because of unique properties: optical, electronic and magnetic [23]. It is widely acknowledged that point defects in crystals such as oxygen vacancies [V_o (i.e., F^+-type center, F^+ center, or F_c)] may alter material efficiency in bare MgO solids [24]. In addition, MgO has lower density as compared to other metal oxides including cupric oxide, zinc oxide and iron oxide [25]. MgO is an alkaline earth metal oxide with a high pH of zero charge [26], surface area ~250–300 m^2/g [27], and zeta potential about − 29.89 mV [28]. Research has found that both particle size and specific surface area are crucial factors that affect the adsorption performance. Hence the surface properties of resulting products are significantly affected by the calcination temperature during synthesis [29–33]. Non-toxic MgO possesses enhanced organic applications as an antibacterial agent for heartburn relief and bone regeneration compared to other Mg compounds as confirmed by U.S. Food and Drug Administration (21CFR184.1431) [34–36].

In the last decade, thick sheet of carbon-based material graphene oxide (GO) has been extensively studied for different applications [37]. Two-dimensional GO nanomaterials demonstrate huge electron mobility, strong chemical stability, wide surface area and high thermal conductivity [38, 39]. Chemical derivative of graphene is GO possessing surface area about 736.6 m^2/g (theoretical) [40] and zeta potential value of − 113.77 mV [41] containing epoxide, carboxylic and hydroxyl groups. These functional groups result in a negative charge, and hydrophilicity and readily produce GO dispersion in aqueous solution to build a stable suspension [42, 43].

Furthermore, several studies have looked into textile dye degradation for MgO, where MgO was prepared via thermal decomposition and used for methylene blue degradation. 90% of this dye degraded after 180 min [44]. Also, MgO was prepared through a sol–gel method with 15–25 nm particle size, for elimination of 98.3% of dye in wastewater after 300 min [45]. The purpose in this study is to check the influence of GO dopant on MgO, for which various wt. ratios (0, 0.01, 0.03, and 0.05) of GO was doped into MgO using chemical precipitation method. Effects of dopant GO on different characteristics of MgO such as structural, morphological and chemical composition in catalysis and antibacterial action were studied. On the other hand, motivation behind the use of these nanocomposites is to explore the significant use of plasmonic nanomaterials to enhance the antimicrobial as well as catalytic activity of metal oxides.

Experimental Section

Materials

Magnesium chloride ($MgCl_2{\cdot}6H_2O$, 99%), sodium nitrate ($NaNO_3$, 98%) and sodium hydroxide (NaOH, 98%) were procured from Sigma Aldrich. Graphite powder (99.5%), sulfuric acid (H_2SO_4) and potassium permanganate ($KMnO_4$, 99.5%) were procured from Analar.

Synthesis of Magnesium Oxide and Graphene Oxide

By following the wet chemical co-precipitation strategy, GO-doped MgO was prepared. The modified Hummer method [46] was used in the preparation of GO. To prepare MgO, desired amount of $MgCl_2{\cdot}6H_2O$ (0.5 M) were stirred into 50 mL of deionized water (DI water) on hot plate. The pH of stirred solution was maintained at 12 using NaOH (0.1 M), which was stirred for 4 h at 80 °C. Stirred solution was centrifuged at 3500 rpm for 15 min

subsequently; supernatant was collected and dried at 120 °C for 24 h in the oven. Collected powder was ground using mortar and pestle to achieve fine powders of undoped and GO (0.01, 0.03 and 0.05) doped MgO. The schematic diagram of GO-doped MgO preparation is shown in Fig. 1.

Catalysis

Catalytic activity of GO-doped MgO nanostructures was tested against 3 mL MBCF (methyl blue ciprofloxacin) mixed in 400 µL of freshly prepared $NaBH_4$ (reducing agent). NaOH and H_2SO_4 (400 µL) were added to obtain basic and acidic nature of solution, respectively. After that, 400 µL of doped MgO was added in based solution of reducing agent. Later, blue color of prepared dye (MBCF) started to faint indicating dye degradation of MBCF into Leuco-MBCF (colorless). Samples received from faint solution at various intervals were captured with UV–Vis spectrophotometer in 200–800 nm range as shown in Fig. 2.

Isolation and Identification of *S. aureus* and *E. coli*

Specimens of mastitis positive sheep milk were retrieved from many veterinary clinics and farms in Punjab and cultured on sheep blood agar (SBA) 5%. Overnight at 37 °C, cultural samples were incubated. Segregated bacterial isolates were purified by streaking on MacConkey and mannitol salt agar (MA and MSA) in triplets maintaining ~ pH 7, respectively. Validation of standard colonies proceeded with gram stain and biochemical analysis (i.e., catalase and coagulase tests).

Antibacterial Activity

Antibacterial behavior of synthesized material was assessed through well diffusion assay with swabbing 0.5 McFarland of isolated *E. coli* and *S. aureus* bacterial strains on MA and MSA, respectively. A sterile cork borer was used to form wells with a diameter of 6 mm on the MA and MSA plates and distinct concentrations of pure and doped MgO (0.5 and 1.0 mg/0.5 mL) were loaded into each well as minimum and maximum dose in comparison with ciprofloxacin (0.005 mg/0.5 mL) and DI water (0.55 mL) as positive and negative controls, respectively, under aseptic conditions. After an overnight incubation at 37 °C, antimicrobial effectiveness was achieved by calculating inhibition areas in millimeters (mm) using the Vernier caliper.

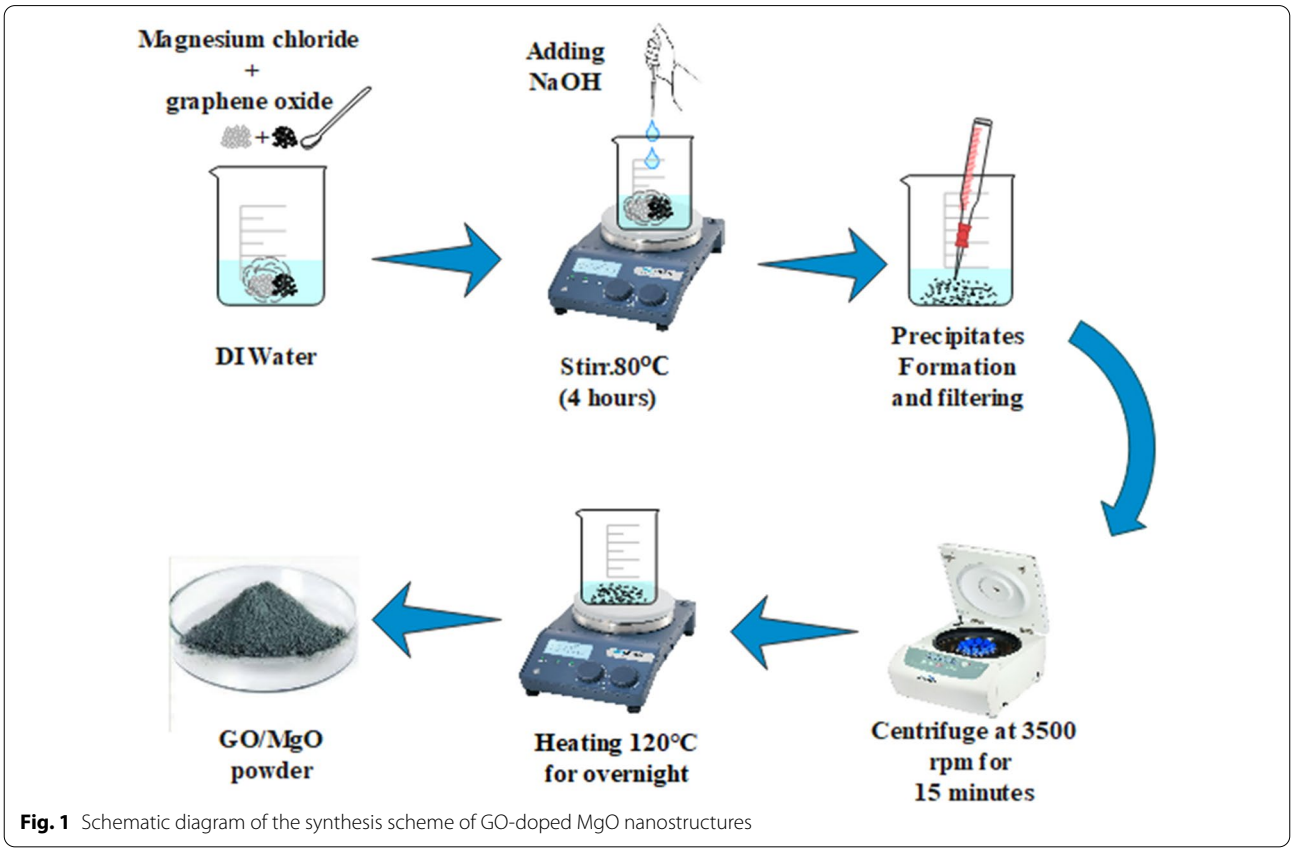

Fig. 1 Schematic diagram of the synthesis scheme of GO-doped MgO nanostructures

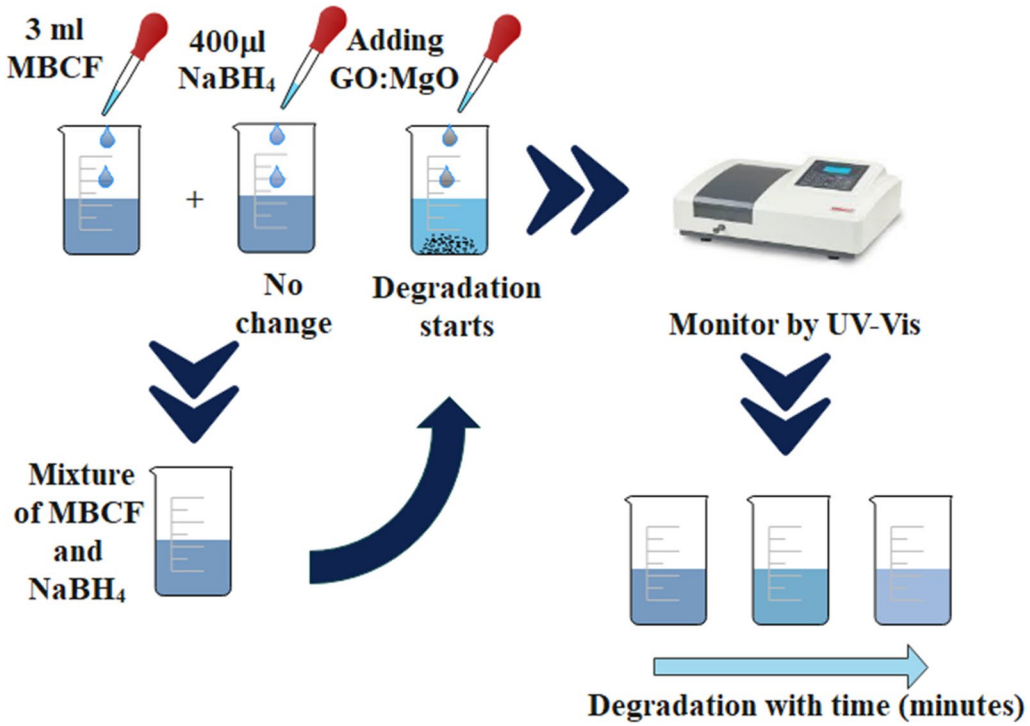

Fig. 2 Schematic representation of catalytic activity during dye degradation

Statistical Analysis

A one-way analysis of variation (ANOVA) with SPSS 20 was used to estimate antimicrobial effectiveness in terms of inhibition zone scores (mm).

Materials Characterization

To identify the crystal structure and phases in the prepared products, the samples were assessed through X-ray diffractometer (model: PAN Analytical Xpert–PRO) using Cu-Kα radiation ($\lambda = 1.540$ Å) and 2θ values from 10° to 85°. Study of attached functional groups was acquired through FTIR (Perkin Elmer spectrometer) used in 4000–400 cm^{-1} range. Absorption spectra were recorded with UV–Vis spectrophotometer (Genesys 10S) in the 200–700 nm range, while using a spectrofluorometer (JASCO, FP-8300), photoluminescence (PL) spectroscopy was performed. Raman Spectra are measured with DXR Raman microscope (Thermo Scientific) using laser based at $\lambda = 532$ nm (6 mV). Elemental composition was attained via SEM–EDS using INCA EDS software, whereas d-spacing was visualized with the help of high resolution transmission electron microscope (HR-TEM model JEOL JEM 2100F).

Results and Discussion

XRD of MgO and GO-doped MgO was conducted to identify the crystal structure, size and phase composition in Fig. 3a. Observed peaks at $2\theta° = 37°$, 43.10°, 62.5°,

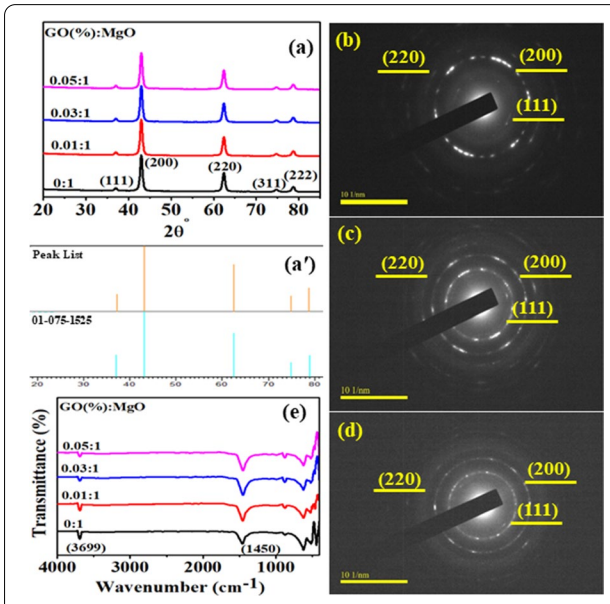

Fig. 3 **a** XRD pattern of GO-doped MgO, **a′** Reference code of MgO, **b** SAED pattern of (0:1), **c** GO (0.01:1, **d** (0.05:1), **e** FTIR spectra

74.7° and 78.8° were in agreement with (111), (200), (220), (311) and (222) planes confirming that MgO had cubic structure coinciding with (JCPDS 75-1525) [47]. Upon doping, diffraction peaks were identical pointing toward the small content of used dopant GO, which was not detectable. Average crystallite size was calculated from diffraction peaks using the Debye–Scherrer equation, which was found to be 13.28 nm. Calculated d-spacing (0.21 nm) was attributed to (200) lattice plane of cubic MgO. Selected area electron diffraction (SAED) patterns of the samples indicated the MgO crystalline nature (Fig. 3b–d). The bright spot of the concentric rings related well with the XRD planes of MgO [48].

In order to examine the attached functional groups of doped MgO, FTIR was operated in the wavenumber from 4000 to 400 cm^{-1} range as illustrated in Fig. 3e. Transmittance peak around 3699 cm^{-1} in doped MgO was ascribed to characteristic stretching vibration of hydroxyl groups (alcohol) obtained due to reaction between MgO surface and water vapors in air [3]. The reduction in peak intensity with the introduction of GO was observed, which is attributed to dopant sheets wrapped around MgO. The band found at 1450 cm^{-1} was related to asymmetric stretching vibrations of carbonate ions (C–O), while the corresponding bending vibration peaks were noticed at ~865 and ~867 cm^{-1} [48]. However, decrease in intensity of afore-mentioned bands was observed for GO-doped MgO sample [20]. Band found around 443 cm^{-1} showing the presence of Mg-O characterized stretching vibration [49].

Absorption spectra of dopant-free and doped MgO were collected from 220 to 700 nm range (Fig. 4a). Band absorption for MgO found at ~250 and ~320 nm can be endorsed to oxygen vacancies (F and F_2^{2+}) centers, respectively. At an excitation $\lambda = 250$ nm, F center photoionization process is involved, led by the equation $F + h\upsilon \leftrightarrow F+ + e$ [23]. Absorption peak of GO was found around 230 nm which can be assigned to π–π^* transitions of C=C in the amorphous carbon system [50], upon doping absorption increased accompanied by redshift. Band gap decreased slightly (5.0–4.8 eV) with increasing amount of GO in fixed amount of MgO as depicted in Fig. 4b. This redshift suggests morphological effects on crystals having numerous active sites or may be quantum confinement effect [51].

Figure 4c reveals PL emission spectra of doped MgO measured ranging from 377 to 500 nm with an exciting λ of 350 nm. To determine the recombination efficiency of charge carriers (migration) and efficacy of trapping, PL was utilized. PL emission peak at 414 nm results from the defect band transition due to energy levels produced with various F (oxygen ion vacancy) type anion vacancies [52]. PL emission of GO is usually attributable to

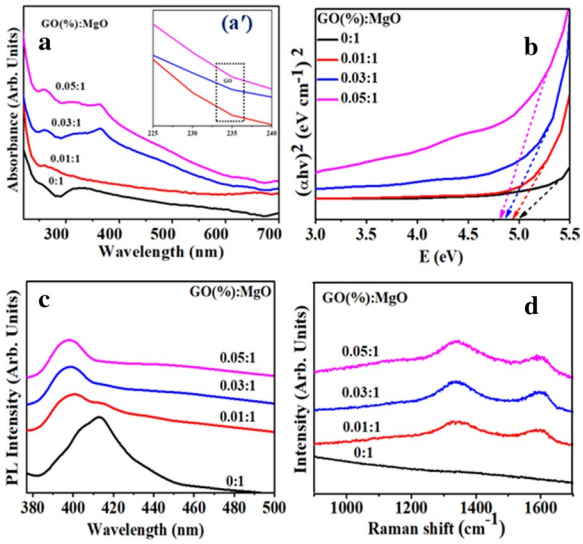

Fig. 4 **a** Absorption spectra of different samples of GO-doped MgO, **a′** Zoomed absorption spectra of GO-MgO, **b** Tauc plot, **c** PL spectra and **d** Raman spectra of GO-MgO nanostructures

electron–hole recombination from adjacent confined electronic states to broad-range valance band (VB) and bottom of conduction band (CB). In atomic structure, emission mostly generates from electronic transitions among the non-oxidized carbon region (–C=C–) and edge of oxidized carbon atom region (C–O, C=O and O=C–OH) [53]. GO-MgO peaks revealed blueshift and exhibited low intensity, which indicated reduced rate of recombination that might be due to transfer of electron from higher energy level to new generated states.

Surface structure and disorder of fabricated samples were analyzed via Raman spectroscopy as presented in Fig. 4d. The control sample spectrum of Raman did not showed any characteristic peak in 100–1600 cm^{-1} region, which suggests low phonons of MgO scattering intensity [54, 55]. In case of doped samples, bands located around 1338 cm^{-1} (D band) and 1598 cm^{-1} (G band) confirmed presence of GO in the sample [56]. D-band is assigned to defect in sp^3 carbon (C) atoms and G-band is arising from E_{2g} phonon scattering (1st order scattering) of sp^2 C atoms. Intensity enhancement of D and G peaks is obtained with increased doping concentration. Moreover, intensity ratio (I_D/I_G) of D and G band indicated disorder degree of sp^2 C domains [46].

To confirm the crystal structure and morphology of doped MgO, HR-TEM was employed (Fig. 5). HRTEM image (5a) of dopant-free sample has agglomerated hexagon shaped nanostructure. With incorporation of GO, hexagon morphology of nanostructure were merged with GO nanosheets and formation of rod-type structure in

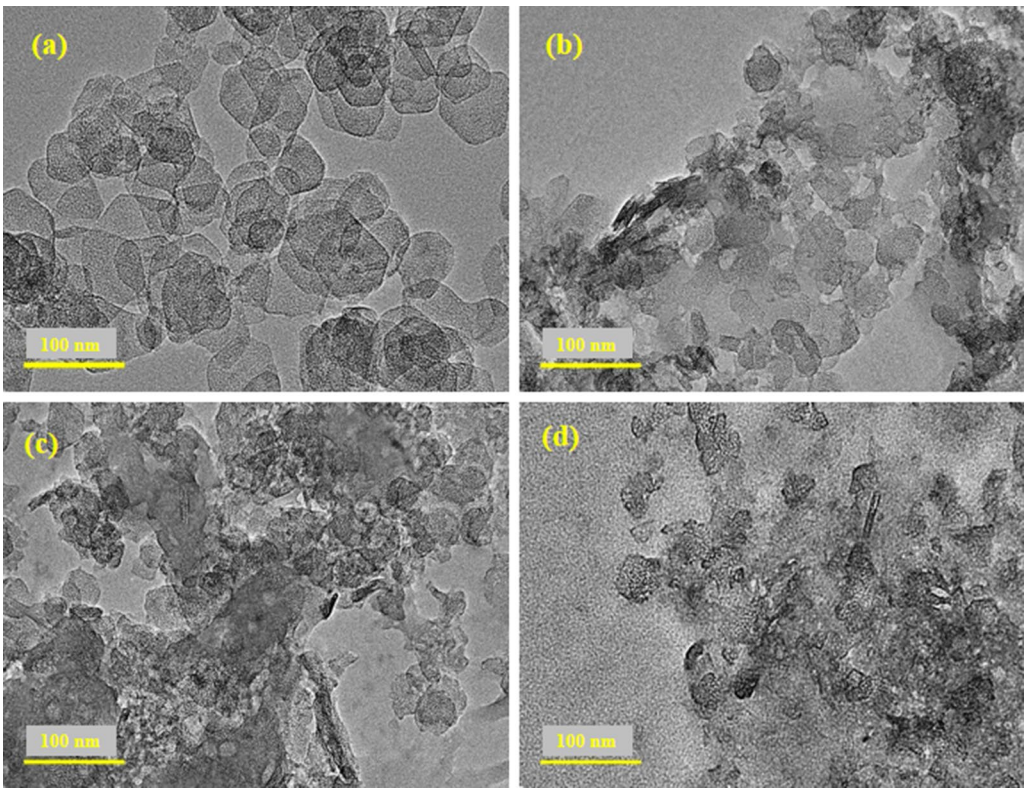

Fig. 5 **a**–**d** HR-TEM images of various concentrations of GO-doped MgO (0, 0.01, 0.03 and 0.05), respectively

the presence of hexagons was observed. The aggregation increased with increasing amount of dopant in MgO where rods and hexagon morphology of nanostructures were found. It is noteworthy that diameter of hexagon nanostructure decreased with higher concentration of GO confirming the interaction between MgO and GO.

Interlayer d-spacing was measured with HR-TEM images using Gatan software as illustrated in Fig. 6a–d. The d-spacing values for various concentrations (0:1, 0.01:1, 0.03:1 and 0.05:1) of GO-doped MgO were calculated as 0.250, 0.240, 0.20 and 0.24 nm, respectively, assigned to (200) plane of MgO (Fig. 6a–d) as synchronized with XRD results. Moreover, change in d-spacing values has been assigned to GO doping into MgO lattices.

SEM–EDS analysis disclosed the detailed information on sample surface regarding its elemental composition. EDS spectra of MgO and various ratios (0.01:1, 0.03:1 and 0.05:1) of GO into MgO are expressed in Fig. 7a–d, respectively. The presence of magnesium (Mg) and oxygen (O) detected in Fig. 7a are confirmation to MgO formation. Carbon (C) peak was ascribed to GO nanosheets, while Na elemental peak in samples was observed due to use of NaOH during synthesis process to maintain pH.

To test the catalytic activity of GO-doped MgO, UV–Vis absorption spectra attained upon reference sample degradation (MBCF) were used. Reducing capacity of $NaBH_4$ with MBCF was not significantly affected after 200 min as demonstrated in Fig. 8a–d. In neutral condition, MBCF (3 mL) solution added into 400 µL $NaBH_4$ and 3 mL samples within 180–160 min showed limited reduction (4.8% degradation) for undoped and doped samples. Moreover, in basic activity for samples (0:1, 0.01:1, 0.03:1, 0.05:1) resulted 11, 3.5, 12, 26% degradation in 3 min, respectively (Fig. 8a–d). Highest catalytic function was obtained in acidic solution with higher concentration (0.05) of GO in MgO nanostructures showing 45% degradation in 1 min as depicted in Fig. 8d.

During catalysis, reduction in MBCF in the presence of $NaBH_4$, synthesized materials act as electron relay such that transfer of electron from BH_4^- ions (donor) to MBCF (acceptor) results in the reduction in dye [57]. Abundant active sites of nanostructures enhanced adsorption for BH_4^- ions and dye molecules to react with each other. Solution pH also affects performance of degradation. For acidic medium (H_2SO_4), catalytic activity enhanced which is attributed to increased generation of H^+ ions offered to be adsorbed on the surface of nanostructure. Upon addition of NaOH for basic medium, the number of hydroxyl groups increases leading to oxidation of reduced products and decrease in catalytic activity.

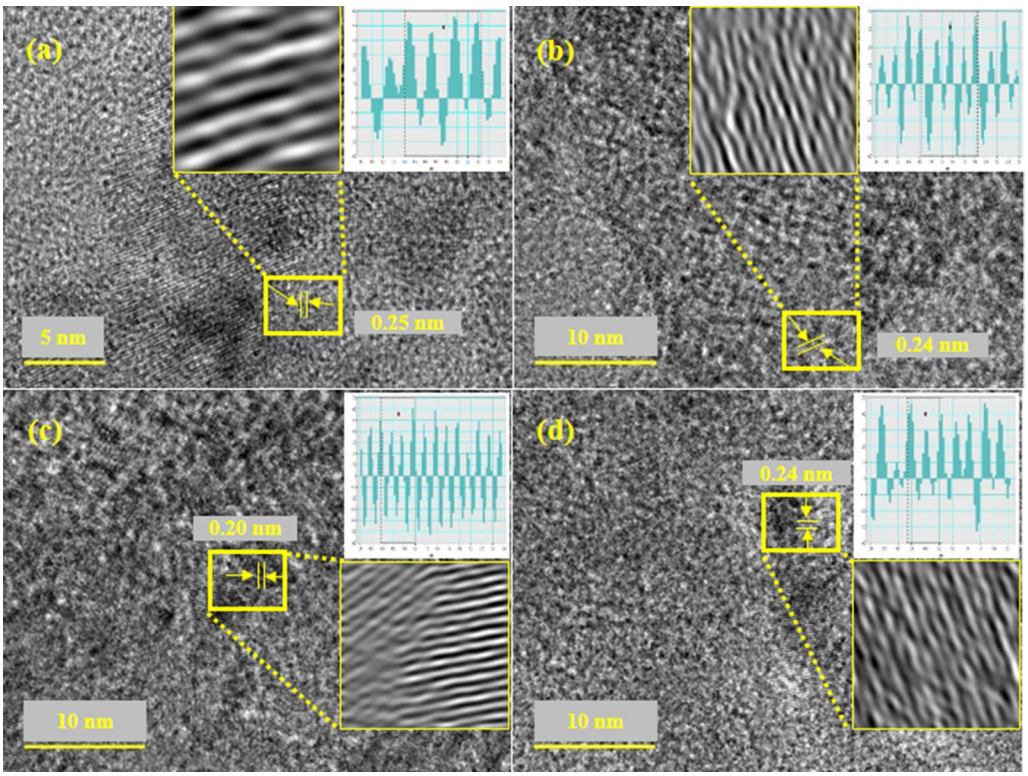

Fig. 6 d-spacing calculated using HR-TEM images of GO-MgO (**a**–**d**) with GO content (0, 0.01, 0.03, 0.05)

Results showed that dye degradation by nanostructures under acidic medium was much higher compared to basic condition.

The in vitro antibacterial efficacy of pure and GO-doped MgO was performed against G −ve and +ve isolates by well diffusion assay (Table 1). Results depicted improved microbicidal action and synergism of GO-MgO for *E. coli* in comparison with *S. aureus*, see Table 1. Significant ($p < 0.05$) inhibition areas were recorded as (1.55–4.75 mm) and (2.10–4.85 mm) for *E. coli* at minimum and maximum dose, respectively, and (1.30–4.00 mm) for *S. aureus* at high dose. All concentrations showed zero antibacterial efficacy for *S. aureus* at low dose. Results comparison proceeded with −ve control DI water (0 mm) and +ve control ciprofloxacin (7.15 mm) and (11.25 mm) inhibition areas for *E. coli* and *S. aureus*, respectively.

Overall, doped nanostructures revealed zero bactericidal activity towards G +ve in low dose, while effectiveness towards G −ve was substantial ($p < 0.05$) relative to G +ve in doped content.

The oxidative stresses of engineered nanostructures rely on diverse factors such as shape, size and concentration of nanoparticles which play an important role in antibacterial action [58]. Small nano-sized materials efficiently produce reactive oxygen species (ROS) causing damage of bacteria cell membrane and extrusion of cytoplasm, resulting bursting of bacteria, see Fig. 9 [59]. Secondly, significant nanomaterial cationic interference with negative bacterial cell membrane fragments result in collapse. Antibacterial activity of MgO nanoparticle enhanced against E. coli, which was on account of the generation of a large amount of O_2^- and may be lipid peroxidation and ROS [60]. In dopant sample, antibacterial activity increased due to increasing GO concentration.

Samples	Control sample band gap (eV)	Decreasing in band gap (eV)	References
GO-doped ZnO	3.6	2.9	[61]
Ag-doped GO	4.10	3.50	[2]
GO-doped ZnO	3.10	2.98	[62]
GO-doped MgO	5.0	4.8	Present study

Conclusion

In the present work, GO-doped MgO nanostructures were successfully synthesized with chemical precipitation route. The cubic structure of MgO was observed using XRD technique and confirmed with HRTEM.

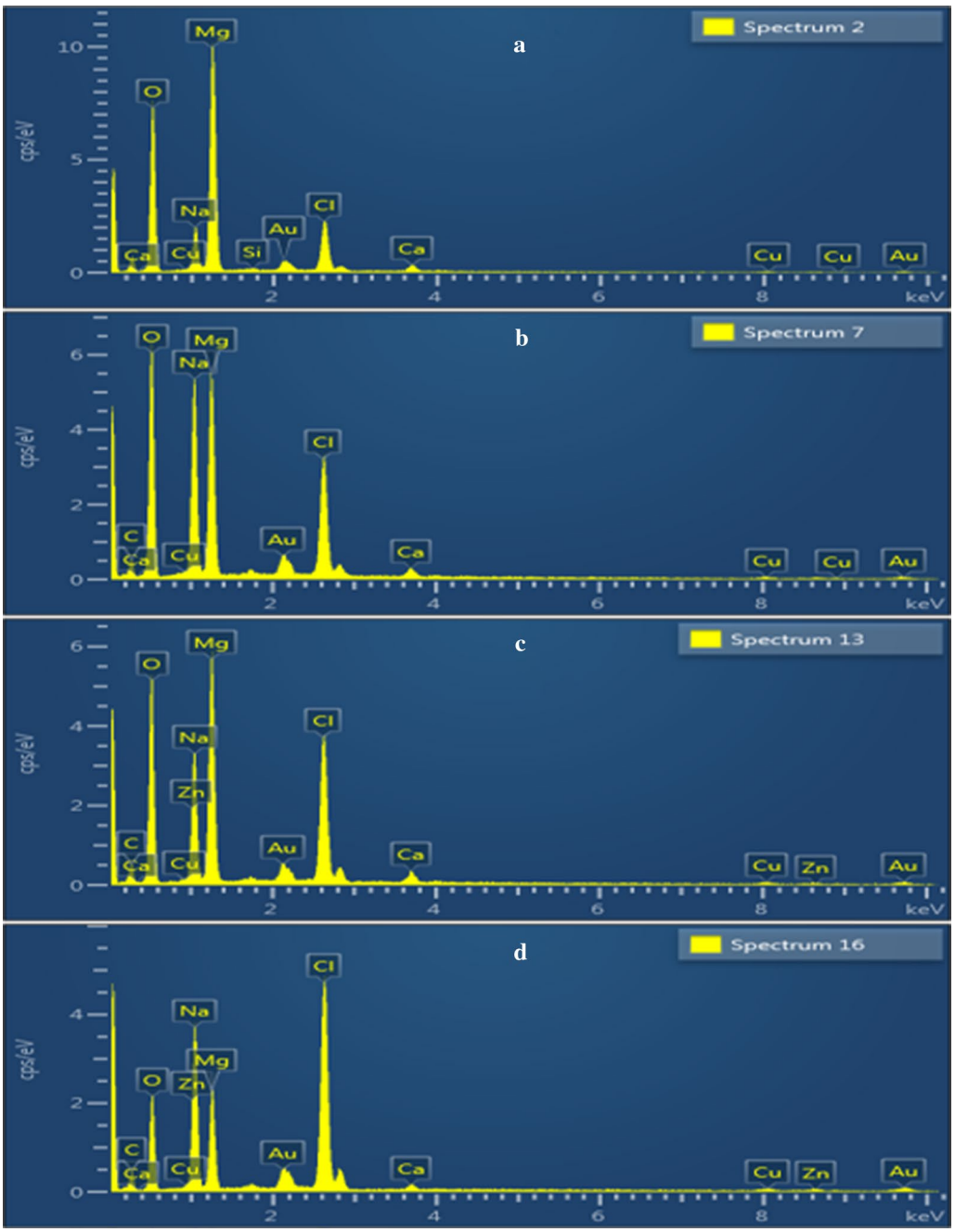

Fig. 7 SEM–EDS analysis of GO-doped MgO (**a**–**d**) with GO content (0, 0.01, 0.03 and 0.05), respectively

Molecular bonding of Mg-O with various functional groups and characteristic transmittance peaks of MgO around 443 cm^{-1} in fingerprint region were recorded using FTIR. The absorption increased upon doping, which introduced redshift at higher concentrations of GO. Calculated band gap using Tauc plot from absorption spectra of doped MgO found to be 4.8 eV (high concentration) comparative to MgO (5.0 eV) was ascribed to redshift in absorption upon doping. Cubic and hexagon morphology of nanostructures was observed in MgO and growth of rod-like structures was observed upon doping with a decrease in diameter of hexagons in HR-TEM. Furthermore, average d-spacing (0.23 nm) from HRTEM with Gatan software are well matched with XRD. EDS analysis revealed elemental composition that showed confirmation of Mg, O with GO doping. With

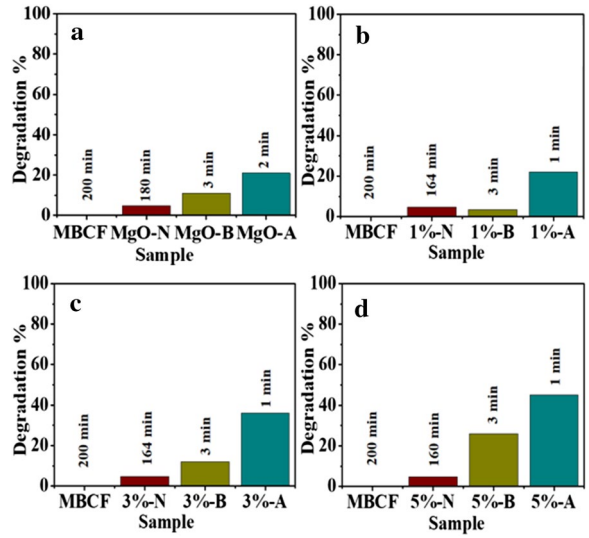

Fig. 8 **a**–**d** Catalysis of blank MBCF and GO-doped MgO in different dye medium [neutral (N), basic (B) and acidic (A)], respectively

Table 1 Antibacterial activity of GO-doped MgO

Sample	Inhibition zone[a] (mm)		Inhibition zone[b] (mm)	
	0.5 mg/50 µL	1.0 mg/50 µL	0.5 mg/50 µL	1.0 mg/50 µL
MgO	0	1.30	1.55	2.10
GO/MgO 1%	0	2.25	2.60	3.35
GO/MgO 3%	0	3.15	3.80	4.40
GO/MgO 5%	0	4.00	4.75	4.85
Ciprofloxacin	11.25	11.25	7.15	7.15
DI water	0	0	0	0

[a] Inhibition zones diameters (mm) for *S. aureus*

[b] Values of zones of inhibition for *E. coli*

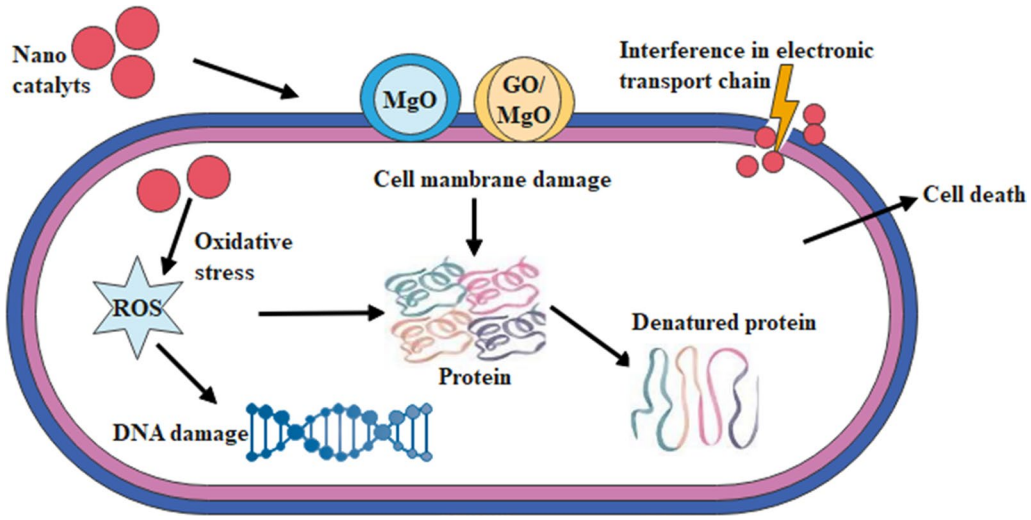

Fig. 9 Proposed mechanism of bactericidal activity GO-MgO nanostructures

the incorporation of GO, intensity of PL decreased from 414 nm accompanied with a blueshift indicating low recombination rate of excitons. The presence of D and G band (at 1338, 1598 cm^{-1}, respectively) associated with sp^3 and sp^2 C atom were verified with Raman. Catalytic activity was assessed and highest dye degradation of about 45% was attained in acidic condition by 0.05 GO-MgO. In addition, experimental results showed enhanced bactericidal efficacy of GO-MgO against G −ve (*E. coli*) relative to G+ve (*S. aureus*). In addition, synergism of GO-MgO showed enhanced bactericidal efficacy against G −ve (*E. coli*) compared to G+ve (*S. aureus*). This study explored the dopant-dependent properties of MgO nanocomposites that can be employed to clean industrial polluted water and in antimicrobial applications for environmental remediation.

Abbreviations

EDS: Energy-dispersive X-ray spectroscopy; FTIR: Fourier transform infrared spectroscopy; FESEM: Field emission scanning electron microscopy; G+ve: Gram-positive; G −ve: Gram negative; GO: Graphene; HR-TEM: High resolution transmission electron microscopy; JCPDS: Joint committee on powder diffraction standards; MgO: Magnesium oxide; UV–Vis: Ultra-violet–visible spectroscopy; XRD: X-ray diffraction.

Acknowledgements

Support provided by the Core Research Facilities at the King Fahd University of Petroleum & Minerals, Dhahran, Saudi Arabia is greatly appreciated.

Authors' contributions
MI and TI performed the whole experiments and TI wrote the manuscript. AH and RG provided the novel idea to carry out the experiment. AH performed antimicrobial and participated in the data analysis of the results and discussion portion. JH, WN and AS reviewed the manuscript, corrected the English. AR and AShahbaz discussed the results and discussion. AUH carried out the FESEM and HRTEM analysis. All authors read and approved the final manuscript.

Funding
Authors are thankful to Higher Education Commission, HEC Pakistan through start research grant project # 21-1669/SRGP/R&D/HEC/2017 Pakistan for financial support.

Availability of data and materials
All data are fully available without restriction.

Declarations

Competing interests
Authors confirm no conflict of interest.

Author details
[1] Solar Cell Application Research Lab, Department of Physics, Government College University Lahore, Lahore 54000, Punjab, Pakistan. [2] Physics Department, Lahore Garrison University, Lahore 54000, Punjab, Pakistan. [3] Department of Clinical Medicine and Surgery, University of Veterinary and Animal Sciences, Lahore 54000, Punjab, Pakistan. [4] Core Research Facilities, King Fahd University of Petroleum & Minerals, Dhahran 31261, Saudi Arabia. [5] Tianjin Institute of Industrial Biotechnology, Chinese Academy of Sciences, Tianjin 300308, China. [6] School of Chemical and Energy Engineering, Faculty of Engineering, Universiti Teknologi Malaysia, 81310 Skudai, Johor, Malaysia. [7] Department of Chemistry, Quaid-i-Azam University, Islamabad 45320, Pakistan. [8] Department of Physics, Government College University Lahore, 54000 Lahore, Pakistan. [9] Department of Physics, Riphah Institute of Computing and Applied Sciences (RICAS), Riphah International University, 14 Ali Road, Lahore, Pakistan.

Received: 9 February 2021 Accepted: 24 March 2021
Published online: 07 April 2021

References

1. Wang Z, Wu A, Ciacchi LC, Wei G (2018) Recent advances in nanoporous membranes for water purification. Nanomaterials 8(2):65. https://doi.org/10.3390/nano8020065
2. Ikram M, Raza A, Imran M, Ul-Hamid A, Shahbaz A, Ali S (2020) Hydrothermal synthesis of silver decorated reduced graphene oxide (rGO) nanoflakes with effective photocatalytic activity for wastewater treatment. Nanoscale Res Lett 15(1):1–10. https://doi.org/10.1186/s11671-020-03323-y
3. Dervin S, Dionysiou DD, Pillai SC (2016) 2D nanostructures for water purification: graphene and beyond. Nanoscale 8(33):15115–15131. https://doi.org/10.1039/c6nr04508a
4. Ali H, Khan E, Ilahi I (2019) Environmental chemistry and ecotoxicology of hazardous heavy metals: environmental persistence, toxicity, and bioaccumulation. J Chem. https://doi.org/10.1155/2019/6730305
5. Sukhadeorao Dongre R (2020) Lead: toxicological profile, pollution aspects and remedial solutions. Lead Chem. https://doi.org/10.5772/intechopen.93095
6. Heidarizad M, Şengör SS (2016) Synthesis of graphene oxide/magnesium oxide nanocomposites with high-rate adsorption of methylene blue. J Mol Liq 224:607–617. https://doi.org/10.1016/j.molliq.2016.09.049
7. Melvin SS, Abigail EA, Chidambaram R (2015) Biosorption of Cr(VI) by *Ceratocystis paradoxa* MSR2 Using isotherm modelling, kinetic study and optimization of batch parameters using response surface methodology. PLoS ONE 10(3):1–23. https://doi.org/10.1371/journal.pone.0118999
8. Samuel MS, Shah SS, Bhattacharya J, Subramaniam K, Pradeep Singh ND (2018) Adsorption of Pb(II) from aqueous solution using a magnetic chitosan/graphene oxide composite and its toxicity studies. Int J Biol Macromol 115:1142–1150. https://doi.org/10.1016/j.ijbiomac.2018.04.185
9. Samuel MS, Shah SS, Subramaniyan V, Qureshi T, Bhattacharya J, Pradeep Singh ND (2018) Preparation of graphene oxide/chitosan/ferrite nanocomposite for Chromium(VI) removal from aqueous solution. Int J Biol Macromol 119:540–547. https://doi.org/10.1016/j.ijbiomac.2018.07.052
10. Samuel M, Abigail EA, Chidambaram R (2015) Isotherm modelling, kinetic study and optimization of batch parameters using response surface methodology for effective removal of Cr(VI) using fungal biomass. PLoS ONE 10(3):1–15. https://doi.org/10.1371/journal.pone.0116884
11. Abigail EA, Samuel MS, Chidambaram R (2015) Hexavalent chromium biosorption studies using *Penicillium griseofulvum* MSR1 a novel isolate from tannery effluent site: Box–Behnken optimization, equilibrium, kinetics and thermodynamic studies. J Taiwan Inst Chem Eng 49:156–164. https://doi.org/10.1016/j.jtice.2014.11.026
12. Omar FS, Nay Ming H, Hafiz SM, Ngee LH (2014) Microwave synthesis of zinc oxide/reduced graphene oxide hybrid for adsorption-photocatalysis application. J Photoenergy Int. https://doi.org/10.1155/2014/176835
13. Abigail MEA, Samuel SM, Ramalingam C (2015) Addressing the environmental impacts of butachlor and the available remediation strategies: a systematic review. Int J Environ Sci Technol 12(12):4025–4036. https://doi.org/10.1007/s13762-015-0866-2
14. Samuel MS, Bhattacharya J, Parthiban C, Viswanathan G, Pradeep Singh ND (2018) Ultrasound-assisted synthesis of metal organic framework for the photocatalytic reduction of 4-nitrophenol under direct sunlight. Ultrason Sonochem 49:215–221. https://doi.org/10.1016/j.ultsonch.2018.08.004
15. Samuel MS et al (2020) Green synthesis of cobalt-oxide nanoparticle using jumbo Muscadine (*Vitis rotundifolia*): characterization and photo-catalytic activity of acid Blue-74. J Photochem Photobiol B Biol 211:112011. https://doi.org/10.1016/j.jphotobiol.2020.112011
16. Datta S, Veena R, Samuel MS, Selvarajan E (2021) Immobilization of laccases and applications for the detection and remediation of pollutants: a review. Environ Chem Lett 19(1):521–538. https://doi.org/10.1007/s10311-020-01081-y
17. Samuel MS, Jose S, Selvarajan E, Mathimani T, Pugazhendhi A (2020) Biosynthesized silver nanoparticles using *Bacillus amyloliquefaciens*; application for cytotoxicity effect on A549 cell line and photocatalytic degradation of p-nitrophenol. J Photochem Photobiol B Biol 202:111642. https://doi.org/10.1016/j.jphotobiol.2019.111642
18. Krishnan K. Effect of microstructures and textures on the anisotropy of mechanical properties of AZ31 magnesium alloy sheets subjected to high strain rate rolling. J Phys D Appl Phys. 2019;0–31 (**in press**).
19. Zheng Y, Cao L, Xing G, Bai Z, Huang J, Zhang Z (2019) Microscale flower-like magnesium oxide for highly efficient photocatalytic degradation of organic dyes in aqueous solution. RSC Adv 9(13):7338–7348. https://doi.org/10.1039/C8RA10385B
20. Yang S et al (2015) Hierarchical flowerlike magnesium oxide hollow spheres with extremely high surface area for adsorption and catalysis. J Mater Chem A 4(2):400–406. https://doi.org/10.1039/c5ta08542j
21. Shuai HL, Huang KJ, Zhang WJ, Cao X, Jia MP (2017) Sandwich-type microRNA biosensor based on magnesium oxide nanoflower and graphene oxide–gold nanoparticles hybrids coupling with enzyme signal amplification. Sens Actuators B Chem 243:403–411. https://doi.org/10.1016/j.snb.2016.12.001
22. Li M, Zhou S, Xu M (2017) Graphene oxide supported magnesium oxide as an efficient cathode catalyst for power generation and wastewater treatment in single chamber microbial fuel cells. Chem Eng J 328:106–116. https://doi.org/10.1016/j.cej.2017.07.031
23. Pathak N, Ghosh PS, Gupta SK, Kadam RM, Arya A (2016) Defects induced changes in the electronic structures of MgO and their correlation with the optical properties: a special case of electron–-hole recombination from the conduction band. RSC Adv 6(98):96398–96415
24. Li JM, Hu YB (2019) O_2 atmospheric annealing-tunable defects in ionic oxide MgO nanoribbons. Appl Phys Lett 114(20):203101. https://doi.org/10.1063/1.5099244
25. Paquin F, Rivnay J, Salleo A, Stingelin N, Silva C (2015) Multi-phase semicrystalline microstructures drive exciton dissociation in neat plastic semiconductors. J Mater Chem C 3:10715–10722. https://doi.org/10.1039/b000000x

26. Nagpal M, Kakkar R (2020) Facile synthesis of mesoporous magnesium oxide–graphene oxide composite for efficient and highly selective adsorption of hazardous anionic dyes. Res Chem Intermed 46(5):2497–2521. https://doi.org/10.1007/s11164-020-04103-0
27. Bartley JK, Xu C, Lloyd R, Enache DI, Knight DW, Hutchings GJ (2012) Simple method to synthesize high surface area magnesium oxide and its use as a heterogeneous base catalyst. Appl Catal B Environ 128:31–38. https://doi.org/10.1016/j.apcatb.2012.03.036
28. Behzadi E et al (2019) Albumin binding and anticancer effect of magnesium oxide nanoparticles. Int J Nanomedicine 14:257–270. https://doi.org/10.2147/IJN.S186428
29. Samuel MS, Subramaniyan V, Bhattacharya J, Parthiban C, Chand S, Singh NDP (2018) A GO-CS@MOF [Zn(BDC)(DMF)] material for the adsorption of chromium(VI) ions from aqueous solution. Compos. Part B Eng 152(vi):116–125. https://doi.org/10.1016/j.compositesb.2018.06.034
30. Abigail EA, Samuel MS, Chidambaram R (2016) Application of rice husk nanosorbents containing 2,4-dichlorophenoxyacetic acid herbicide to control weeds and reduce leaching from soil. J Taiwan Inst Chem Eng 63:318–326. https://doi.org/10.1016/j.jtice.2016.03.024
31. Samuel MS, Subramaniyan V, Bhattacharya J, Chidambaram R, Qureshi T, Pradeep Singh ND (2018) Ultrasonic-assisted synthesis of graphene oxide—fungal hyphae: an efficient and reclaimable adsorbent for chromium(VI) removal from aqueous solution. Ultrason Sonochem 48(vi):412–417. https://doi.org/10.1016/j.ultsonch.2018.06.012
32. Samuel MS, Selvarajan E, Subramaniam K, Mathimani T, Seethappan S, Pugazhendhi A (2020) Synthesized β-cyclodextrin modified graphene oxide (β-CD-GO) composite for adsorption of cadmium and their toxicity profile in cervical cancer (HeLa) cell lines. Process Biochem 93:28–35. https://doi.org/10.1016/j.procbio.2020.02.014
33. Samuel MS, Suman S, Selvarajan E, Mathimani T, Pugazhendhi A (2020) Immobilization of Cu3(btc)2 on graphene oxide-chitosan hybrid composite for the adsorption and photocatalytic degradation of methylene blue. J Photochem Photobiol B Biol 204:111809. https://doi.org/10.1016/j.jphotobiol.2020.111809
34. Bhattacharya P, Swain S, Giri L, Neogi S (2019) Fabrication of magnesium oxide nanoparticles by solvent alteration and their bactericidal applications. J Mater Chem B 7(26):4141–4152. https://doi.org/10.1039/c9tb00782b
35. Rajendran V, Deepa B, Mekala R (2018) Studies on structural, morphological, optical and antibacterial activity of Pure and Cu-doped MgO nanoparticles synthesized by co-precipitation method. Mater Today Proc 5(2):8796–8803. https://doi.org/10.1016/j.matpr.2017.12.308
36. Krishnamoorthy K, Moon JY, Hyun HB, Cho SK, Kim SJ (2012) Mechanistic investigation on the toxicity of MgO nanoparticles toward cancer cells. J Mater Chem 22(47):24610–24617. https://doi.org/10.1039/c2jm35087d
37. Amirov RR, Shayimova J, Nasirova Z, Dimiev AM (2017) Chemistry of graphene oxide. Reactions with transition metal cations. Carbon N Y 116:356–365. https://doi.org/10.1016/j.carbon.2017.01.095
38. Apul OG, Wang Q, Zhou Y, Karanfil T (2013) Adsorption of aromatic organic contaminants by graphene nanosheets: comparison with carbon nanotubes and activated carbon. Water Res 47(4):1648–1654. https://doi.org/10.1016/j.watres.2012.12.031
39. Xiao L, Damien J, Luo J, Jang HD, Huang J, He Z (2012) Crumpled graphene particles for microbial fuel cell electrodes. J Power Sources 208:187–192. https://doi.org/10.1016/j.jpowsour.2012.02.036
40. Montes-Navajas P, Asenjo NG, Santamaría R, Menéndez R, Corma A, García H (2013) Surface area measurement of graphene oxide in aqueous solutions. Langmuir 29(44):13443–13448. https://doi.org/10.1021/la4029904
41. Şimşek B, Ultav G, Korucu H, Yartaşi A (2018) Improvement of the graphene oxide dispersion properties with the use of TOPSIS based Taguchi application. Period Polytech Chem Eng 62(3):323–335. https://doi.org/10.3311/PPch.11412
42. Moussavi G, Hossaini Z, Pourakbar M (2016) High-rate adsorption of acetaminophen from the contaminated water onto double-oxidized graphene oxide. Chem Eng J 287:665–673. https://doi.org/10.1016/j.cej.2015.11.025
43. Deng JH, Zhang XR, Zeng GM, Gong JL, Niu QY, Liang J (2013) Simultaneous removal of Cd(II) and ionic dyes from aqueous solution using magnetic graphene oxide nanocomposite as an adsorbent. Chem Eng J 226:189–200. https://doi.org/10.1016/j.cej.2013.04.045
44. Salehifar N, Zarghami Z, Ramezani M (2016) A facile, novel and low-temperature synthesis of MgO nanorods via thermal decomposition using new starting reagent and its photocatalytic activity evaluation. Mater Lett 167:226–229. https://doi.org/10.1016/j.matlet.2016.01.015
45. Jorfi S et al (2016) Enhanced coagulation-photocatalytic treatment of Acid red 73 dye and real textile wastewater using UVA/synthesized MgO nanoparticles. J Environ Manag 177:111–118. https://doi.org/10.1016/j.jenvman.2016.04.005
46. Aqeel M et al (2019) TiO_2@RGO (reduced graphene oxide) doped nanoparticles demonstrated improved photocatalytic activity. Mater Res Express 6(8):086215. https://doi.org/10.1088/2053-1591/ab244a
47. Wang H, Li G, Fakhri A (2020) Fabrication and structural of the Ag_2S-MgO/graphene oxide nanocomposites with high photocatalysis and antimicrobial activities. J Photochem Photobiol B Biol 207:111882. https://doi.org/10.1016/j.jphotobiol.2020.111882
48. Chowdhury IH, Chowdhury AH, Bose P, Mandal S, Naskar MK (2016) Effect of anion type on the synthesis of mesoporous nanostructured MgO, and its excellent adsorption capacity for the removal of toxic heavy metal ions from water. RSC Adv 6(8):6038–6047. https://doi.org/10.1039/c5ra16837f
49. Li LX, Xu D, Li XQ, Liu WC, Jia Y (2014) Excellent fluoride removal properties of porous hollow MgO microspheres. New J Chem 38(11):5445–5452. https://doi.org/10.1039/c4nj01361a
50. Rabchinskii MK et al (2016) Nanoscale perforation of graphene oxide during photoreduction process in the argon atmosphere. J Phys Chem C 120(49):28261–28269. https://doi.org/10.1021/acs.jpcc.6b08758
51. Bindhu MR, Umadevi M, Kavin Micheal M, Arasu MV, Abdullah Al-Dhabi N (2016) Structural, morphological and optical properties of MgO nanoparticles for antibacterial applications. Mater Lett 166:19–22. https://doi.org/10.1016/j.matlet.2015.12.020
52. Balamurugan S, Ashna L, Parthiban P (2014) Synthesis of nanocrystalline MgO particles by combustion followed by annealing method using hexamine as a fuel. J Nanotechnol 2014:10–12. https://doi.org/10.1155/2014/841803
53. Goumri M, Venturini JW, Bakour A, Khenfouch M, Baitoul M (2016) Tuning the luminescence and optical properties of graphene oxide and reduced graphene oxide functionnalized with PVA. Appl Phys A Mater Sci Process 122(3):1–8. https://doi.org/10.1007/s00339-016-9725-3
54. Wu M et al (2017) Catalytic performance of MgO-supported Co catalyst for the liquid phase oxidation of cyclohexane with molecular oxygen. Catalysts 7(5):155. https://doi.org/10.3390/catal7050155
55. Cazzanelli E, Kuzmin A, Mariotto G, Mironova-Ulmane N (2003) Study of vibrational and magnetic excitations in NicMg1-cO solid solutions by Raman spectroscopy. J Phys Condens Matter 15(12):2045–2052. https://doi.org/10.1088/0953-8984/15/12/321
56. Xu J, Xu D, Zhu B, Cheng B, Jiang C (2018) Adsorptive removal of an anionic dye Congo red by flower-like hierarchical magnesium oxide (MgO)-graphene oxide composite microspheres. Appl Surf Sci 435:1136–1142. https://doi.org/10.1016/j.apsusc.2017.11.232
57. Fairuzi AA, Bonnia NN, Akhir RM, Abrani MA, Akil HM (2018) Degradation of methylene blue using silver nanoparticles synthesized from imperata cylindrica aqueous extract. IOP Conf Ser Earth Environ Sci 105(1):012018. https://doi.org/10.1088/1755-1315/105/1/012018
58. Navale GR, Rout CS, Gohil KN, Dharne MS, Late DJ, Shinde SS (2015) Oxidative and membrane stress-mediated antibacterial activity of WS2 and rGO-WS2 nanosheets. RSC Adv 5(91):74726–74733. https://doi.org/10.1039/c5ra15652a
59. Ikram M et al (2020) Dye degradation performance, bactericidal behavior and molecular docking analysis of Cu-doped TiO_2 nanoparticles. RSC Adv 10(41):24215–24233. https://doi.org/10.1039/d0ra04851h
60. Tang ZX, Lv BF (2014) MgO nanoparticles as antibacterial agent: Preparation and activity. Braz J Chem Eng 31(3):591–601. https://doi.org/10.1590/0104-6632.20140313s00002813
61. Lin Y, Hong R, Chen H, Zhang D, Xu J (2020) Green synthesis of ZnO-GO composites for the photocatalytic degradation of methylene blue. J Nanomater 20:20. https://doi.org/10.1155/2020/4147357
62. Boukhoubza I et al (2020) Graphene oxide concentration effect on the optoelectronic properties of ZnO/GO nanocomposites. Nanomaterials 10(8):1–16. https://doi.org/10.3390/nano10081532

Publisher's Note